

# Hydrogen etching and cutting of multiwall carbon nanotubes

Michael J. Behr, E. Ashley Gaulding, K. Andre Mkhoyan, and Eray S. Aydil<sup>a)</sup>

*Department of Chemical Engineering and Materials Science, University of Minnesota, Minneapolis, Minnesota 55455*

(Received 14 May 2010; accepted 13 September 2010; published 25 October 2010)

The interaction of H atoms with the curved concentric graphene walls of a multiwall carbon nanotube and the stacked planar graphene sheets of graphite was investigated using a combination of high resolution transmission electron microscopy (HRTEM) in conjunction with electron energy-loss and Raman spectroscopies. Continuous cylindrical graphene walls of a nanotube are etched and amorphized by the H atoms. Etching is not uniform across the length of the CNT but rather, small etch pits form at defective sites on the CNT walls along the entire nanotube length. Once an etch pit is formed, etching proceeds rapidly, and the remainder of the CNT is quickly etched away. The carbon K core-loss edge spectra collected from etch pits do not differ from the spectra collected from pristine CNT walls, indicating that reactions occur exclusively at the exposed graphene edges. Similar observations were made when sheets of planar graphite were exposed to H atoms. Confocal Raman spectroscopic measurements revealed that H etching occurs preferentially at the graphite edges. Eventually, large holes appear in the graphite, as observed under HRTEM. Etched holes in planar graphite are similar to the etch pits that form when a graphene layer is rolled up to form the cylindrical walls of a CNT. Once a hole or an etch pit is formed, the edges of the planar graphene sheets or cylindrical CNT walls become exposed, and H etching proceeds quickly from these edges. © 2010 American Vacuum Society. [DOI: 10.1116/1.3498737]

## I. INTRODUCTION

A fundamental understanding of the interactions of atomic and molecular hydrogen with nanostructured carbon materials, such as carbon nanotubes (CNTs), graphite, and graphene, is important for several reasons. First, hydrogen is ubiquitous during the synthesis of these materials using methods such as plasma-enhanced chemical vapor deposition (PECVD).<sup>1</sup> A fundamental understanding of the interactions of H with CNTs and graphene layers can lead to an improved understanding of the role of H during their synthesis. Second, CNTs and graphene have been suggested as potential hydrogen storage materials.<sup>2</sup> Finally, hydrogen has the ability to change both the electronic properties and the atomic arrangements of carbon atoms in these nanostructured carbon materials. For example, it has been shown that addition of hydrogen to a hydrocarbon precursor gas is required to grow well-graphitized CNTs; changing the amount of hydrogen present during growth drastically affects the structure of the carbon nanotubes.<sup>3–11</sup> Specifically, we showed, recently, that the highest quality multiwall carbon nanotubes (MWCNTs) with the narrowest diameter distribution were produced when H<sub>2</sub> and CH<sub>4</sub> were added in equal proportions to the plasma. On the other hand, if the H<sub>2</sub>-to-CH<sub>4</sub> ratio in the feed gas is too high, CNTs do not grow.<sup>3</sup>

Exposure to a H<sub>2</sub> plasma can drastically change the electronic properties of CNTs. Zhang *et al.*<sup>12</sup> found that exposure of single-walled CNTs (SWCNTs) to a rf hydrogen plasma for 3 min created various C–H<sub>x</sub> species on the CNT side walls and resulted in a significant decrease in its electrical

conductance. Density functional theory calculations show that the band gap of a SWCNT can be changed dramatically through the hydrogenation of its graphene walls.<sup>13</sup> Similar electronic changes are observed when a single layer of graphite, also known as graphene, is hydrogenated. Upon hydrogenation, the normally highly conductive semimetal graphene is transformed into an insulator.<sup>14</sup> Hydrogenation, and hence the changes in the electronic properties, has been found to be completely reversible by heating to ~450–600 °C.<sup>14–16</sup>

The atomic structure of a CNT can also undergo severe physical distortions and even structural changes when H atoms interact with its cylindrical graphene wall(s). This is the case when the flux of H atoms is much larger than the modest H-atom fluxes present during CNT synthesis from CH<sub>4</sub>/H<sub>2</sub> gas mixtures. For example, Muniz *et al.*<sup>17</sup> studied the effects of hydrogen chemisorption using molecular dynamics simulations and found that upon hydrogenation, CNTs expand with increasing H coverage. When the H dose and H-atom exposure temperature is increased, irreversible structural changes to the CNT structure can begin.<sup>18</sup> For example, Zhang *et al.*<sup>12</sup> observed that when plasma power or H-exposure time was increased, CNTs were cut and etched. Rao *et al.*<sup>19</sup> found that SWCNTs were easily etched by H<sub>2</sub> at 900 °C but remained unaffected at 800 °C.

In addition to etching, interactions with H atoms have also been predicted to induce structural rearrangements in the layered graphene nanotube and planar graphite structures. For example, a variety of crystalline carbon phases, such as diamond<sup>20</sup> and other hydrogenated crystalline carbon phases,<sup>21</sup> have been predicted to form as a result of repeated interactions between H atoms and the concentric graphene

<sup>a)</sup>Author to whom correspondence should be addressed; electronic mail: aydil@umn.edu

walls of a multi walled CNT (MWCNT). Experiments by Sun *et al.*<sup>22</sup> and Yang *et al.*<sup>23</sup> suggest that indeed H-atom exposure can transform MWCNTs to diamonds. Unfortunately, these reports lack the atomic-scale chemical analysis needed to show unambiguously that the observed crystals are indeed composed of carbon.

In this study, we use atomic-scale chemical analysis, specifically electron energy-loss spectroscopy (EELS), coupled with high-resolution transmission electron microscopy (HR-TEM), and confocal Raman spectroscopy to systematically investigate the evolution of MWCNTs and planar graphite when they are exposed to H atoms generated through electron-impact dissociation in a H<sub>2</sub> plasma.

## II. EXPERIMENT

MWCNTs used in this study were grown using a radio-frequency (rf) (at 13.56 MHz) inductively coupled plasma and iron catalyst through PECVD, as described in a previous publication.<sup>24</sup> CNTs grew to  $\sim 4$   $\mu\text{m}$  in length, diameters ranged from  $\sim 25$ – $35$  nm, and the number of concentric graphene walls was typically greater than 20. CNT films were sonicated briefly in ethanol to remove them from the silicon substrate, and then dispersed from solution on amorphous silicon nitride membrane window TEM grids, obtained from SPI Supplies, Inc. For comparison, we also purchased and used MWCNTs from Catalytic Materials LLC. These CNTs had outer diameters ranging from 9 to 24 nm, and were typically composed of ten or more concentric graphene walls. The third material studied was graphite. For these studies, highly oriented pyrolytic graphite (HOPG) disks, grade SPI-3, which exhibit a mosaic angle  $\sim 3.5^\circ \pm 1.5^\circ$ , and an average grain size of 30–40 nm were obtained from SPI Supplies Inc.

CNTs and HOPG disks were exposed to hydrogen atoms created by electron-impact dissociation of H<sub>2</sub> in a H<sub>2</sub>:Ar [50:2.5 SCCM (SCCM denotes cubic centimeter per minute at STP (SCCM))] plasma maintained with 200 W rf power in the same inductively coupled plasma reactor used for CNT growth.<sup>25</sup> Hydrogen atom exposures were conducted over a substrate temperature range of 25–725 °C, and over a pressure range of 0.15–1 Torr, in increments of 15 min. To prevent ion bombardment, the plasma source was located approximately 25 cm above the substrate platen, while a grounded stainless-steel mesh immediately above the substrate prevented electric fields from forming a plasma immediately above the substrate. As a result, the sample was not irradiated with ions or electrons during plasma exposure. During H<sub>2</sub> plasma exposure at 0.15 Torr, we determined the H-atom flux to the substrate to be  $2.2 \times 10^{17}$  cm<sup>-2</sup> s<sup>-1</sup> using a method based on measuring the changes in the free-electron concentration in a polycrystalline ZnO thin film as a result of H incorporation, with Fourier-transform infrared spectroscopy. The details of this method are given in the Appendix.

The temperature of the resistively heated substrate platen was monitored using a thermocouple, while substrate temperature was calibrated independently by measuring the

temperature-dependent position of the direct band edge of silicon with a spectroscopic ellipsometer. During H-exposure at 25 °C, the substrate heater was turned off; the thermocouple typically measured a temperature of 30 °C after 15 min of H-atom exposure.

CNTs and HOPG disks were examined for structural changes after each 15 min increment of H-exposure with HRTEM and EELS using FEI Tecnai F30 (S)TEM with a Schottky field emission electron gun operated at 300 keV and equipped with a bottom-mounted Gatan Ultrascan 4000 SP digital CCD camera, and Gatan 2002 GIF spectrometer. All samples were held under a heat lamp for approximately 1 h to drive off and decompose hydrocarbons before inserting them into the microscope. Unique markings on the TEM grids enabled us to return to and examine the same nanotube after each 15 min H-exposure. We typically kept track of numerous nanotubes but only show representative results here. In addition to HRTEM images, EELS spectra of the carbon *K*-edge, with onset at  $\sim 285$  eV, were measured at multiple locations along the lengths of over 30 MWCNTs from each sample. During EELS acquisition, the electron beam was defocused, such that the beam diameter was slightly larger than the diameter of the CNT. The purpose of using a slightly spread beam was (i) to reduce the incident electron beam current density to prevent beam-induced damage to the CNT walls, and (ii) to sample the entire diameter of the nanotube, in order to average out changes in the C *K*-edge fine structure as a result of the inherent continuously changing orientation of the CNT graphene walls relative to the incident electron beam.<sup>26</sup> At each location, five EELS spectra were collected using a 1 s integration time, which were then averaged to improve the signal-to-noise ratio. This brief exposure did not damage the CNT walls: the fine structure of the C *K*-edge remained constant. A camera length of 470 mm, and a 2 mm spectrometer entrance aperture yielded a collection semiangle of 1.53 mrad and were kept constant throughout this entire study. An energy dispersion of 0.3 eV/channel was used. The energy resolution, measured as the full-width-at-half maximum of the zero-loss peak was  $\sim 1.2$  eV.

All EELS spectra were processed individually within Gatan DIGITAL MICROGRAPH and ORIGINLAB software packages. The slowly decreasing background present in all spectra, arising from multiple inelastic scattering events, was subtracted from each C *K*-edge by fitting the pre-edge background over a 60 eV wide window to an inverse power law function  $I = AE^{-r}$ , where the fitting parameter *r* ranged from 2 to 5.<sup>27</sup> Relative changes to the  $\pi^*$  and  $\sigma^*$  peaks at  $\sim 285.5$  and  $\sim 292.5$  eV,<sup>28</sup> respectively, were calculated by integrating the intensity under the peaks over a 1.5 eV wide window, centered around the maximum of each peak. No detectable amorphous carbon was found to build up as a result of the brief electron beam exposures used in this study.

Average HOPG structure was further characterized using Raman spectroscopy. Raman spectra of the HOPG disks from face and edge locations were collected using a Witec alpha300R Raman spectrometer in the confocal backscatter-

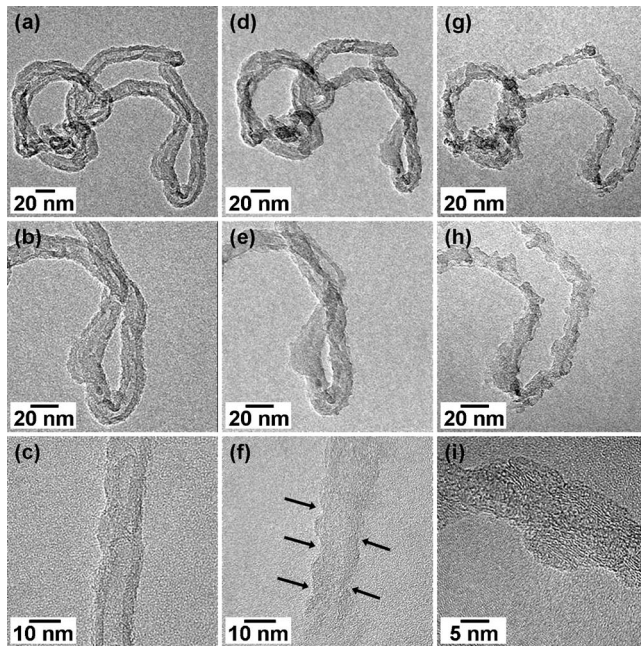


FIG. 1. (a)–(c) in the first column show the BF-TEM images of segments of a MWCNT before H-atom exposure. (d)–(f) show the same segments after 15 min of H-atom exposure at room temperature. Nanotube walls show increased roughness due to formation of etch pits as indicated in (f). (g)–(i) show the same segments after a total H-atom exposure of 30 min. Numerous deep etch pits are observed along the nanotube lengths. Some regions are also now amorphous. The CNT shown in each panel is the same CNT across any row.

ing geometry. Raman spectra were collected in triplicates from different regions and averaged results are presented. An argon ion laser (514.5 nm wavelength) operating at 20 mW and focused to  $\sim 1 \mu\text{m}$  spot provided excitation. Raman scattering was detected using a DV401 CCD Peltier-cooled detector.

### III. RESULTS AND DISCUSSION

#### A. Observations with TEM

Examining individual MWCNTs with TEM after each 15 min increment of H-atom exposure revealed that H atoms etch and amorphize the concentric graphene walls. Figure 1 shows a collection of bright-field (BF) TEM images of MWCNTs before H-exposure [Figs. 1(a)–1(c)], after 15 min H-exposure [Figs. 1(d)–1(f)], and after 30 min H exposure [Figs. 1(g)–1(i)] at room temperature. The CNT shown in each panel is the same CNT across any row in Fig. 1. The initial CNT structure, before exposure to the H atoms, is already quite defective. In fact, at numerous locations along the nanotube length, interior walls are connected to form cups perpendicular to the nanotube axis. Additionally, many graphene walls are oriented at an angle relative to the CNT axis and terminate at the tube exterior, which results in a rough CNT exterior with many exposed graphene edges. After 15 min of H-atom exposure, nanotube exteriors become significantly rougher. Careful examination reveals that at certain locations along the CNT length, small divots, or etch

pits,  $\sim 2 \text{ nm}$  deep are present and cut into the CNT walls. A few such locations are indicated in Fig. 1(f) with arrows. Continued H-exposure for an additional 15 min significantly increases the size and number of these pits along the CNT walls. In some areas in the vicinity of etch pits, the initially crystalline graphitelike CNT structure now lacks long range order and appears amorphous as a result of the H-atom exposure [Fig. 1(i)]. These amorphous regions may contain dangling bonds as well as H-terminated carbon atoms. In Fig. 1(i), some regions of the CNT still exhibit lattice fringes that correspond to the ordered concentric graphene walls, while other regions do not and appear completely disordered. Also evident in Fig. 1 is the decrease in average diameter as a result of carbon removal from the exterior of the CNTs during exposure to H atoms. Upon further H-atom exposure, for a cumulative time of 45 min, CNTs were completely etched from the silicon nitride TEM grid. The etching, or carbon removal rate, was found to increase substantially with increased H-exposure time. In other words, the rate was a function of time and carbon was removed increasingly faster with H-exposure time.

Hydrogen atoms are also found to etch and change the structure of planar sheets of graphite. Experiments with planar graphite sheets further our understanding of the reactions occurring on CNTs. Figure 2 shows the BF-TEM images of HOPG flakes that were exposed to H atoms for 6 h at room temperature. Compared to the etching of MWCNTs over the course of 30 min (Fig. 1), H reactions with HOPG occur much slower. The initially continuous and highly crystalline sheet of graphite appears disordered after 6 h of H-atom exposure and contains numerous holes as a result of the interactions with and etching by H atoms. Most changes were observed near the graphite edges. Some areas appear amorphized, while many sections of the graphite sheet exhibited squiggly lattice fringes either grouped together in small domains, or in pairs, indicating that the graphite structure has been significantly changed. The HOPG flakes before H-atom exposure, as shown in Fig. 2(c), appear completely crystalline and do not exhibit holes. Thinking of the structure of a MWCNT as a rolled-up piece of graphite, holes in the graphite sheet are akin to the etch pits observed in the walls of MWCNTs. If a hole is present in the graphite sheet, then it forms a pit in the CNT walls when the sheet is rolled into a cylinder. These observations suggest that the atomic reactions of H with the ordered graphene networks of planar HOPG and MWCNTs are similar.

The anisotropic and nonuniform nature of graphene layer etching with H is especially evident when higher quality MWCNTs, i.e., nanotubes with continuous walls with no visual structural defects, are exposed to H atoms. Figures 3(a) and 3(b) show BF-TEM images of one such well-graphitized MWCNT that was exposed to a H-plasma for 10 min at  $725^\circ\text{C}$ . After this relatively short H-atom exposure, numerous large etch pits had formed at multiple locations along the nanotube length; in some cases, hydrogen consumed approximately three-fourths of the nanotube diameter. Between etch pits, however, sections of pristine CNT graphene walls

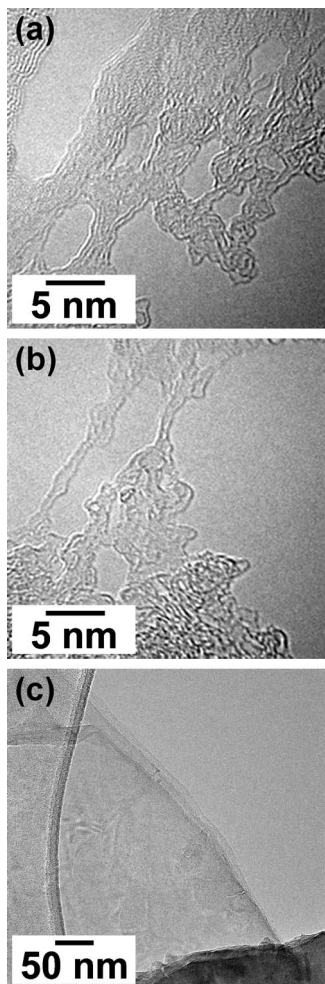


FIG. 2. [(a) and (b)] High-resolution BF-TEM images of different locations along the edge of a HOPG flake after 6 h of H-atom exposure at room temperature. The initially highly crystalline layered HOPG structure is now very disordered, as evident by the random and squiggly lattice fringes, and contains holes. (c) BF-TEM of a HOPG flake before H-atom exposure is highly crystalline and does not contain holes.

still exist; the walls in these regions appeared identical to the pre-exposed CNT. Often, these walls remained pristine until they terminated abruptly to form the edge of the etch pit. Once an etch pit forms, C is preferentially and rapidly removed from the edges of this pit. Consequently, continued H-exposure causes the etch pits to grow quickly both in width and depth. Figures 3(c) and 3(d) show a MWCNT from the same sample after only an additional 2 min (12 min total) of H-exposure at 725 °C. During these additional 2 min, H atoms continued to preferentially react with and remove carbon from the exposed graphene edges of the existing etch pits, causing them to grow larger until the entire diameter of the CNT was cut in half. Figure 3(a) shows a CNT that has been cut into smaller segments by this etching process. Each segment usually contains a region that is still pristine. Occasionally, near the edges of the etch pits, or where the nanotube was cut in half, the CNT walls appear amorphous [see Fig. 3(d)]. It is clear from these observations that H etching occurs faster at the exposed graphene edges

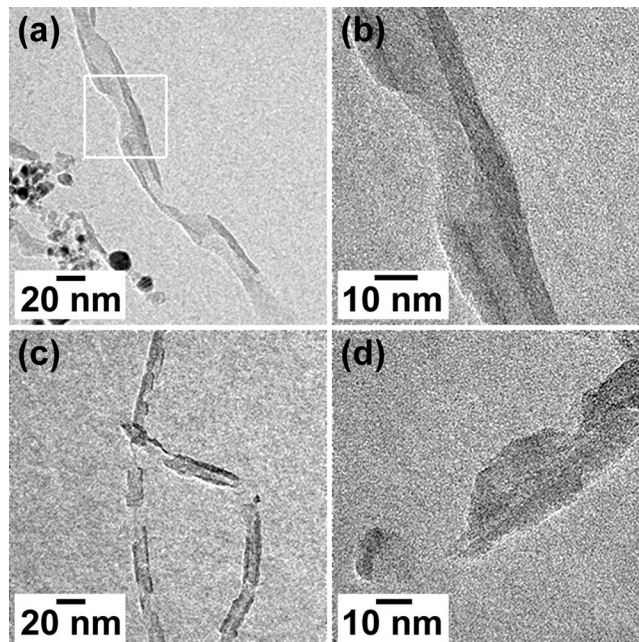


FIG. 3. (a) BF-TEM image of a high-quality, well-graphitized MWCNT that has received 10 min of H-atom exposure at 725 °C. Numerous etch pits are present along the nanotube length; one etch pit is indicated with the white rectangle in (a). (b) Magnified image of the etch pit enclosed by the white rectangle in (a). (c) A MWCNT from the same sample that received an additional 2 min of H-atom exposure. During this short additional exposure, H atoms reacted rapidly at the exposed graphene edges of etch pits to completely cut through the nanotube. (d) A magnified image of a location where the nanotube was cut shows that some of the carbon in this vicinity is amorphous.

within an etch pit while reactions with the continuous pristine graphene basal planes of nanotube walls between etch pits occur slowly.

## B. Raman spectroscopy

Raman spectroscopy was used to probe and compare the changes in the structure of a single piece of HOPG along its basal plane (face) and at its edges when exposed to H atoms from a H<sub>2</sub> plasma. First-order Raman spectra recorded, before H-exposure, from the face and edges of a HOPG disk are shown in Figs. 4(a) and 4(b), respectively. The Raman spectra show two major peaks, a G peak at ~1580 cm<sup>-1</sup> and a D peak at ~1350 cm<sup>-1</sup>.<sup>29,30</sup> The ratio,  $I(D)/I(G)$ , is often used as a measure of the disorder in a graphitic carbon structure, or in the case of graphite, as a measure of its crystallite size or interdefect distance.<sup>30,31</sup> The G peak corresponds to in-plane stretching of  $sp^2$  C–C bonds in rings or chains, while the D peak corresponds to breathing modes of  $sp^2$  C–C bonds in rings only: the D peak is only present when the symmetry of the graphite is broken.<sup>29</sup> The ratio  $I(D)/I(G)$  was calculated from peak heights and displayed on each plot of Fig. 4. Peak heights were used instead of the area under the peak, because it is known that the D peak width increases more than the G peak width with decreasing crystal size.<sup>32</sup> Before H-atom exposure, both spectra are dominated by the G peak at ~1580 cm<sup>-1</sup> [Figs. 4(a) and 4(b)]. The presence

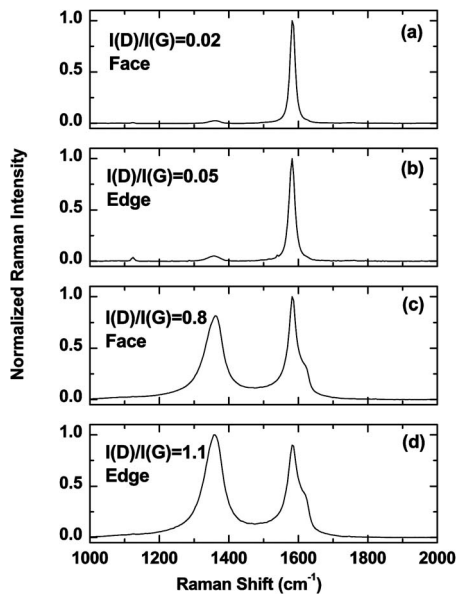


FIG. 4. First-order Raman spectra of a HOPG flake face (a) and edge (b) before H-atom exposure. The intensity ratio  $I(D)/I(G)$  was calculated and is displayed on each plot. Raman spectra obtained from the face (c) and edge (d) of the HOPG flake after 60 min of H-atom exposure at room temperature. The greater increase in the intensity ratio  $I(D)/I(G)$  at the HOPG edge indicates that H preferentially reacts here.

of the  $D$  peak on the face of the HOPG, though small, indicates that the structural order is not perfect even in this HOPG sample. Nevertheless, this gives a reference level for this ratio in a presumably highly ordered and symmetric graphitic structure like HOPG. Intensity ratios,  $I(D)/I(G)$ , of 0.02 and 0.05 were determined from peak heights for the face and edge of the HOPG disk, respectively. Upon H-atom exposure of the HOPG disk for 1 h at room temperature, significant changes to the spectra were observed [Figs. 4(c) and 4(d)]. Specifically, a large increase in both the  $D$  and  $G$  peak widths, and the appearance of a new peak at  $\sim 1617\text{ cm}^{-1}$ , referred to as the  $D'$  peak,<sup>33–35</sup> indicate increased disorder (i.e., defects) and the formation of new crystalline edges.<sup>36–38</sup> Most notable, however, is the dramatic increase in the  $D$ -band intensity at both the face and edge positions on the HOPG disk. The  $D$ -band intensity from the edge of the disk grew significantly and even surpassed the  $G$ -peak height. The  $I(D)/I(G)$  ratio at the HOPG edge after H-atom exposure has increased to 1.1, while at the face of the HOPG disk, it has only increased to 0.8. This larger ratio observed at the graphite edge indicates that a higher level of disorder is present here as compared to the graphite face, as a result of the 1 h of H-atom exposure. This suggests that the exposed edges of graphite are more reactive, and thus H will react at these sites preferentially, causing structural transformations or etching to occur here first. This conclusion is corroborated with TEM images shown in Fig. 2.

### C. Electron energy-loss spectroscopy

To examine the reactions that cause etching and amorphization of the CNT walls, we examined the type of carbon

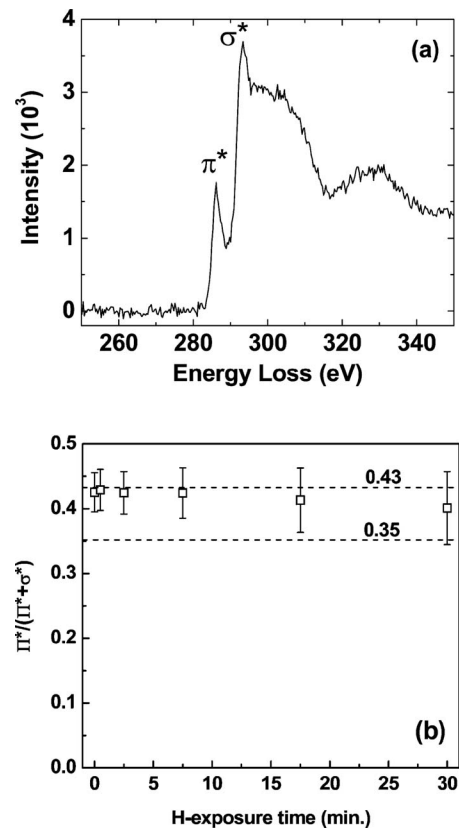


FIG. 5. (a) A representative EELS spectrum of the carbon  $K$ -edge obtained from a MWCNT. The  $\pi^*$  and  $\sigma^*$  peaks are labeled. The incident electron beam was defocused such that the entire diameter of the nanotube was probed. (b) A plot of the  $\pi^*$ -to- $(\pi^*+\sigma^*)$  intensity ratio as measured by integrating over a 1.5 eV wide window centered around each peak, as a function of H-plasma exposure time. This ratio remains constant over the 30 min of H-plasma exposure, which indicates that the amorphous carbon formed remains  $sp^2$ -hybridized.

bonding present as a function of H-atom exposure time using EELS. Specifically, we measured the C  $K$  core-loss edge at numerous etch pits and pristine regions along the lengths of over 30 MWCNTs after each increment of H-atom exposure at room temperature. For this experiment, EELS measurements were made after H exposures of 0.5, 2.5, 7.5, 17.5, and 30 min. A representative EELS spectrum obtained from a MWCNT is shown in Fig. 5(a). There are two primary peaks in the C  $K$  core-loss edge: the  $\pi^*$  peak at 285.5 eV and the  $\sigma^*$  peak at 292.5 eV.<sup>28</sup> The intensity ratio of these two peaks depends on the orientation of the graphitelike CNT walls relative to the incident electron beam and on the hybridization of carbon bonding present.<sup>27,39–41</sup> All spectra were collected with the electron beam defocused, such that the diameter of the beam was larger than the CNT diameter. This practice averages the signal across many ring orientations so that any changes to the  $\pi^*$ -to- $(\pi^*+\sigma^*)$  ratio would be a direct measure of changes in carbon bonding hybridization. Initially, the pristine MWCNTs exhibit purely  $sp^2$ -hybridized carbon bonding. The average  $\pi^*$ -to- $(\pi^*+\sigma^*)$  intensity ratio of MWCNTs before H-exposure, as determined from measurements at various locations on over 30 nanotubes, was 0.43. Any H-induced transformation of carbon bonding to

$sp^3$ -hybridized carbon, either during the etching or amorphization processes, would decrease this ratio from its initial value of 0.43, since a purely  $sp^3$ -bonded sample does not exhibit a  $\pi^*$  peak.<sup>41,42</sup> However, over the course of 30 min of H-atom exposure, no change to the relative intensities of the  $\pi^*$  and  $\sigma^*$  peaks was observed. The plot of Fig. 5(b) shows that the  $\pi^*$ -to- $(\pi^* + \sigma^*)$  ratio as a function of H-exposure time remains unchanged, even though numerous etch pits had formed, and some regions appeared amorphous as a result of the exposure. A typical amorphous carbon material, which is composed of both  $sp^2$ - and  $sp^3$ -bonded carbon, produces an average  $\pi^*$ -to- $(\pi^* + \sigma^*)$  intensity ratio of  $\sim 0.35$ .<sup>43</sup> A change in this magnitude would be easily discernible with EELS. However, the major contribution to the C  $K$ -edge signal comes from the graphene nanotube walls that surround each etch pit because the incident electron beam is defocused. If the edges of an etch pit that appear amorphous are composed of only  $sp^3$ -bonded carbon, we calculate that this would contribute only  $\sim 4\%$  to the total  $K$ -edge signal. Thus, the unchanged  $\pi^*$ -to- $(\pi^* + \sigma^*)$  ratio after H-atom exposure is primarily a measure of the structure of the continuous basal graphene walls of the carbon nanotube that surround each etch pit, and indicates that these carbon atoms remain purely  $sp^2$ -bonded. This further corroborates TEM and Raman observations that H atoms preferentially react and affect the structure of the CNT walls at exposed graphene edges.

#### D. Discussion

The study and comparison of H interactions on planar graphite with H interactions on MWCNTs has offered insights into the observations made during etching of MWCNTs. Graphite is found to be most susceptible to incident H atoms at its exposed edges. Likewise, a carbon nanotube is most susceptible to H atoms at etch pits, where fresh graphene edges are exposed. The observed growth of etch pits and eventual cutting of the CNT diameter is a direct consequence of these sites' higher reactivity.

The initial formation of an etch pit may occur at a site along the outer CNT wall that contains a defect. Atomic-scale defects such as small changes in carbon ring size due to strain or dangling bonds on the outer wall of a MWCNT are not easy to detect even with TEM. However, the appearances of hemispherical etch pits in distinct locations on the MWCNT walls and holes in planar graphene layers in HOPG point to existence of such defect sites that serve as the nucleation site for these pits and holes. Once hydrogen interacts with such defects to expose the edges of the stacked graphene layers, etching reactions proceed very quickly to widen the etch pit or the hole.

Curvature of the graphene CNT walls appears to play a significant role in the speed at which CNTs etch. We observe that thicker CNTs take longer H-atom exposure to etch than do thinner nanotubes, i.e., CNTs with higher curvature etch faster. This observation is consistent with studies by Zhang *et al.* who observed that small-diameter single-wall CNTs exhibit higher hydrogenation reactivity,<sup>44</sup> and are etched and cut more easily by H atoms than thicker diameter tubes.<sup>12</sup>

Planar graphite has no curvature and we find that significantly longer H-atom exposures were needed to etch and transform the planar graphite samples, as compared to the very short H-atom exposures that etched and transformed MWCNTs.

Finally, we carried out a variety of control experiments to show that the observed changes are due to reactive species created by the plasma. Most notably, we heated the carbon nanotubes in  $H_2$  to similar temperatures without the plasma for similar periods of time but we did not observe any changes with the TEM.

#### IV. CONCLUSIONS

The interaction of H atoms with the layered graphene structures in MWCNTs and HOPG was investigated using TEM, Raman spectroscopy, and EELS. Incident H atoms from the  $H_2$  plasma preferentially react at the exposed graphene edges of HOPG flakes, resulting in etching and structural transformations of the carbon atoms. Hydrogen atoms also react at defects present on the face of HOPG layers and etch holes through the HOPG flakes. This same anisotropic etching is also observed when MWCNTs are exposed to H atoms generated in a  $H_2$  plasma. It is observed that H reacts at various locations along the nanotube length to form etch pits into the nanotube walls; once formed, etch pits grow rapidly with further H-exposure because of the large number of exposed graphene edges, until the entire tube diameter is consumed. Often, graphene walls in segments between etch pits remain pristine, while in other cases, graphene layers are amorphous as a result of the H-exposure. Reactions with H atoms occur much faster for MWCNTs than with HOPG, suggesting that curvature increases the reactivity.

#### ACKNOWLEDGMENTS

The authors thank O. Ugurlu for technical support. This material is based primarily on the work supported by the National Science Foundation (NSF), Grant No. CBET-0613629. This work utilized the University of Minnesota Characterization Facility, which receives partial support from the NSF-NNIN program and capital equipment funding from the NSF through the MRSEC program. The H flux monitor work was supported by the Department of Energy Office of Fusion Energy Science, Contract No. DE-SC0001939.

#### APPENDIX

We developed a method for measuring the H-atom flux at the plane of the substrate surface during  $H_2$  plasma exposure. Our method is based on infrared measurements of the change in free-electron absorption in a polycrystalline ZnO film when this film exposed to H atoms. Hydrogen acts as an electron donor in ZnO,<sup>45,46</sup> and thus the concentration of hydrogen-generated free carriers can be extracted from their absorption in the infrared, as demonstrated by Wolden *et al.*<sup>47</sup> The change in the concentration of free carriers can in turn be related to the flux of H atoms impinging on a ZnO film placed on the substrate platen.

A 110 nm thick polycrystalline ZnO thin film was grown from solution on a trapezoidal-shaped GaAs attenuated-total-reflection (ATR) crystal. The beveled edges of the crystal were first masked so that the film was deposited only on the top face. Next, the crystal was placed top-face down in a 0.01M solution of zinc nitrate and methenamine in ethanol. At 80 °C, a 110 nm thick film was grown in 1 h.

The ZnO-coated GaAs ATR crystal was placed on the substrate platen located approximately 25 cm below the rf plasma coil. An IR beam from a Nicolet Magna-IR 550 Fourier transform infrared spectrometer (FTIR) spectrometer was directed into the plasma reaction chamber through KBr windows and focused onto the 45° beveled edge of the GaAs ATR crystal, in which it underwent 31 internal reflections from the top and bottom crystal surfaces, sampling the ZnO film 15 times. After exiting the opposite 45° beveled edge of the ATR crystal, the transmitted beam was detected with an external, cooled HgCdTe detector. Absorption spectra in the range from 650 to 5000 cm<sup>-1</sup> with a spectral resolution of 2 cm<sup>-1</sup> were averaged over 300 scans and recorded after each 20 s exposure to a 200 W H<sub>2</sub>/Ar plasma up to 120 s total exposure. The H<sub>2</sub> and Ar flow rates were 50 and 2.5 SCCM, respectively, and the chamber pressure was 0.15 Torr. All spectra were collected relative to the ZnO-coated ATR crystal before H-exposure so that any measured changes in absorbance were solely due to the incident H atoms from the plasma.

Figure 6 shows the FTIR spectra of the 110 nm thick polycrystalline ZnO on GaAs ATR crystal obtained after every 20 s up to 120 s of total H-atom exposure. The observed broad-band absorption closely follows a wavelength dependence of  $\lambda^2$ , as predicted by the Drude model for free-electron absorption in a polycrystalline semiconductor.<sup>48</sup> The increase in broad-band absorption with longer H-atom exposure is due to the increase in the number of H atoms that become incorporated into the film. This change in carrier concentration was extracted from the frequency dependence of the free-electron absorption and the complex part of the dielectric function using the Drude model and an optical model for the multiple reflections that occur in ATR geometry.<sup>49</sup> In ATR geometry, the extinction coefficient,  $k(\tilde{\nu})$ , is related to the infrared absorbance,  $A(\tilde{\nu})$ , by

$$k(\tilde{\nu}) = \frac{A(\tilde{\nu})}{4\pi\tilde{\nu}N_R d_e(\tilde{\nu})}, \quad (\text{A1})$$

where  $\tilde{\nu}$ ,  $N_R$ , and  $d_e$  are the wavenumber, the number of internal reflections in the internal crystal, and the effective thickness of the ZnO film, respectively. The effective thickness is used here instead of the ZnO film thickness because the IR beam, when reflected from the GaAs-ZnO interface, decays exponentially into the ZnO film.<sup>50</sup> The effective thickness was calculated using the three-layer optical model of the GaAs-ZnO-vacuum stack as presented by Han *et al.*<sup>49</sup> The imaginary component of the dielectric constant,  $\varepsilon_2(\tilde{\nu})$ , is related to the extinction coefficient by  $\varepsilon_2(\tilde{\nu}) = 2nk(\tilde{\nu})$ , where  $n$  is the refractive index of ZnO. Next, the Drude model

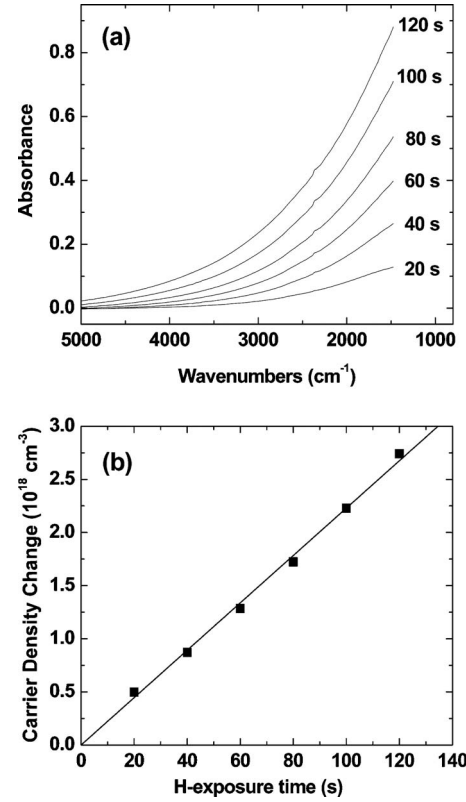


Fig. 6. (a) Infrared absorption spectra, obtained in attenuated-total-reflection mode, of a 110 nm thick polycrystalline ZnO film after 20 s H-atom exposures at room temperature. The broad-band free-electron absorption increases as H atoms from the plasma are incorporated into the film. (b) A plot of the increase in carrier density as calculated from the absorption spectra as a function of the H-atom exposure time. The slope of this plot multiplied by the ZnO film thickness yields the H flux to the film surface,  $2.2 \times 10^{17}$  cm<sup>-2</sup> s<sup>-1</sup>.

relates  $\varepsilon_2(\tilde{\nu})$  to the film conductivity,  $\sigma$ , and carrier relaxation time,  $\tau$ , through

$$\varepsilon_2(\tilde{\nu}) = \frac{\sigma}{\varepsilon_0\omega(\omega^2\tau^2 + 1)}, \quad (\text{A2})$$

where  $\omega$  is the frequency in rad/s ( $\omega = 2\pi c\tilde{\nu}$ ) and  $\varepsilon_0$  is the permittivity of vacuum. Both  $\sigma$  and  $\tau$  were determined from a nonlinear least-squares fit of the experimental data to the Drude model. The increase in carrier concentration,  $N_e$ , could then be calculated from  $\sigma$  and  $\tau$  by

$$N_e = \frac{\sigma m^*}{e^2\tau}, \quad (\text{A3})$$

where  $e$  is the electron charge and  $m^* = 0.32$  is the effective mass of electrons in ZnO.<sup>51</sup> Figure 6(b) shows the calculated carrier concentration as a function of H-atom exposure time. Assuming that all H atoms that reach the ZnO surface incorporate into the film and donate 1 electron, then the flux,  $F_H$ , of H atoms to the surface can be calculated from the slope of the plot in Fig. 6(b) by

$$F_H = \delta \frac{d}{dt} N_e, \quad (\text{A4})$$

where  $\delta=110$  nm is the ZnO film thickness. This method yielded a H-atom flux of  $2.2 \times 10^{17}$  cm<sup>-2</sup> s<sup>-1</sup> for a H<sub>2</sub>:Ar (50:2.5 SCCM) 200 W rf plasma at 0.15 Torr.

- <sup>1</sup>M. Meyyappan, L. Delzeit, A. Cassell, and D. Hash, *Plasma Sources Sci. Technol.* **12**, 205 (2003).
- <sup>2</sup>A. C. Dillon, K. M. Jones, T. A. Bekkedahl, C. H. Kiang, D. S. Bethune, and M. J. Heben, *Nature (London)* **386**, 377 (1997).
- <sup>3</sup>M. J. Behr, E. A. Gaulding, K. A. Mkhoyan, and E. S. Aydil, *J. Appl. Phys.* **108**, 053303 (2010).
- <sup>4</sup>J. B. O. Caughman, L. R. Baylor, M. A. Guillorn, V. I. Merkulov, D. H. Lowndes, and L. F. Allard, *Appl. Phys. Lett.* **83**, 1207 (2003).
- <sup>5</sup>T. Y. Lee *et al.*, *Diamond Relat. Mater.* **12**, 1335 (2003).
- <sup>6</sup>P. E. Nolan, D. C. Lynch, and A. H. Cutler, *J. Phys. Chem. B* **102**, 4165 (1998).
- <sup>7</sup>M. S. Bell, K. B. K. Teo, and W. I. Milne, *J. Phys. D: Appl. Phys.* **40**, 2285 (2007).
- <sup>8</sup>M. Chhowalla, K. B. K. Teo, C. Ducati, N. L. Rupesinghe, G. A. J. Amaratunga, A. C. Ferrari, D. Roy, J. Robertson, and W. I. Milne, *J. Appl. Phys.* **90**, 5308 (2001).
- <sup>9</sup>Y. S. Woo, D. Y. Jeon, I. T. Han, N. S. Lee, J. E. Jung, and J. M. Kim, *Diamond Relat. Mater.* **11**, 59 (2002).
- <sup>10</sup>S. H. Lim, H. S. Yoon, J. H. Moon, K. C. Park, and J. Jang, *Appl. Phys. Lett.* **88**, 033114 (2006).
- <sup>11</sup>L. Delzeit, I. McAninch, B. A. Cruden, D. Hash, B. Chen, J. Han, and M. Meyyappan, *J. Appl. Phys.* **91**, 6027 (2002).
- <sup>12</sup>G. Y. Zhang, P. F. Qi, X. R. Wang, Y. R. Lu, D. Mann, X. L. Li, and H. J. Dai, *J. Am. Chem. Soc.* **128**, 6026 (2006).
- <sup>13</sup>V. Barone, J. Heyd, and G. E. Scuseria, *J. Chem. Phys.* **120**, 7169 (2004).
- <sup>14</sup>D. C. Elias *et al.*, *Science* **323**, 610 (2009).
- <sup>15</sup>A. Nikitin, H. Ogasawara, D. Mann, R. Denecke, Z. Zhang, H. Dai, K. Cho, and A. Nilsson, *Phys. Rev. Lett.* **95**, 225507 (2005).
- <sup>16</sup>H. Zhang, F. W. Meyer, H. M. Meyer, and M. J. Lance, *Vacuum* **82**, 1285 (2008).
- <sup>17</sup>A. R. Muniz, T. Singh, and D. Maroudas, *Appl. Phys. Lett.* **94**, 103108 (2009).
- <sup>18</sup>W. Lisowski, E. G. Keim, A. H. J. van den Berg, and M. A. Smithers, *Carbon* **43**, 1073 (2005).
- <sup>19</sup>F. B. Rao, T. Li, and Y. L. Wang, *Physica E (Amsterdam)* **40**, 779 (2008).
- <sup>20</sup>A. R. Muniz, T. Singh, E. S. Aydil, and D. Maroudas, *Phys. Rev. B* **80**, 144105 (2009).
- <sup>21</sup>T. Singh, M. J. Behr, E. S. Aydil, and D. Maroudas, *Chem. Phys. Lett.* **474**, 168 (2009).
- <sup>22</sup>L. T. Sun, J. L. Gong, Z. Y. Zhu, D. Z. Zhu, S. X. He, Z. X. Wang, Y. Chen, and G. Hu, *Appl. Phys. Lett.* **84**, 2901 (2004).
- <sup>23</sup>Q. Q. Yang, S. L. Yang, C. J. Xiao, and A. Hirose, *Mater. Lett.* **61**, 2208 (2007).
- <sup>24</sup>M. J. Behr, K. A. Mkhoyan, and E. S. Aydil, *ACS Nano* **4**, 5087 (2010).
- <sup>25</sup>S. Agarwal, A. Takano, M. C. M. van de Sanden, D. Maroudas, and E. S. Aydil, *J. Chem. Phys.* **117**, 10805 (2002).
- <sup>26</sup>R. D. Leapman and J. Silcox, *Phys. Rev. Lett.* **42**, 1361 (1979).
- <sup>27</sup>R. F. Egerton, *Electron Energy-Loss Spectroscopy in the Electron Microscope* (Plenum, New York, 1996), pp. 272–277.
- <sup>28</sup>R. D. Leapman, P. L. Fejes, and J. Silcox, *Phys. Rev. B* **28**, 2361 (1983).
- <sup>29</sup>A. C. Ferrari and J. Robertson, *Phys. Rev. B* **61**, 14095 (2000).
- <sup>30</sup>F. Tuinstra and J. L. Koenig, *J. Chem. Phys.* **53**, 1126 (1970).
- <sup>31</sup>A. C. Ferrari, *Solid State Commun.* **143**, 47 (2007).
- <sup>32</sup>A. Cuesta, P. Dhamelincourt, J. Laureyns, A. Martinez-Alonso, and J. M. D. Tascon, *J. Mater. Chem.* **8**, 2875 (1998).
- <sup>33</sup>R. J. Nemanich and S. A. Solin, *Phys. Rev. B* **20**, 392 (1979).
- <sup>34</sup>C. Thomsen and S. Reich, *Phys. Rev. Lett.* **85**, 5214 (2000).
- <sup>35</sup>R. Saito, A. Jorio, A. G. Souza, G. Dresselhaus, M. S. Dresselhaus, and M. A. Pimenta, *Phys. Rev. Lett.* **88**, 207401 (2002).
- <sup>36</sup>A. Sadezky, H. Muckenhuber, H. Grothe, R. Niessner, and U. Poschl, *Carbon* **43**, 1731 (2005).
- <sup>37</sup>Y. Wang, D. C. Alsmeyer, and R. L. McCreery, *Chem. Mater.* **2**, 557 (1990).
- <sup>38</sup>L. G. Cancado, M. A. Pimenta, B. R. A. Neves, M. S. S. Dantas, and A. Jorio, *Phys. Rev. Lett.* **93**, 4 (2004).
- <sup>39</sup>G. Y. Zhang *et al.*, *Proc. Natl. Acad. Sci. U.S.A.* **102**, 16141 (2005).
- <sup>40</sup>Y. Lifshitz, *Diamond Relat. Mater.* **12**, 130 (2003).
- <sup>41</sup>K. Saitoh, K. Nagasaka, and N. Tanaka, *J. Electron Microsc.* **55**, 281 (2007).
- <sup>42</sup>S. D. Berger, D. R. McKenzie, and P. J. Martin, *Philos. Mag. Lett.* **57**, 285 (1988).
- <sup>43</sup>R. F. Egerton and M. J. Whelan, *J. Electron Spectrosc. Relat. Phenom.* **3**, 232 (1974).
- <sup>44</sup>P. J. Fallon and L. M. Brown, *Diamond Relat. Mater.* **2**, 1004 (1993).
- <sup>45</sup>C. G. Van de Walle, *Phys. Rev. Lett.* **85**, 1012 (2000).
- <sup>46</sup>C. Kılıç and A. Zunger, *Appl. Phys. Lett.* **81**, 73 (2002).
- <sup>47</sup>C. A. Wolden, T. M. Barnes, J. B. Baxter, and E. S. Aydil, *J. Appl. Phys.* **97**, 043522 (2005).
- <sup>48</sup>J. I. Pankove, *Optical Processes in Semiconductors* (Prentice-Hall, Englewood Cliffs, NJ, 1971), pp. 74–76.
- <sup>49</sup>S. M. Han and E. S. Aydil, *J. Appl. Phys.* **83**, 2172 (1998).
- <sup>50</sup>N. J. Harrick, *Internal Reflection Spectroscopy* (Interscience, New York, 1967), p. 17.
- <sup>51</sup>T. Minami, *MRS Bull.* **25**, 38 (2000).